

Saturn's northern auroras and their modulation by rotating current systems during late northern spring in early 2014

J. Kinrade¹, S. V. Badman¹, G. Provan², S. W. H. Cowley², L. Lamy³, A. Bader¹

¹Physics Department, Lancaster University, Lancaster, Bailrigg, UK.

²Department of Physics and Astronomy, University of Leicester, Leicester, UK.

³LESIA, Observatoire de Paris, CNES, PSL, Meudon, France.

Corresponding author: Joe Kinrade (j.kinrade@lancaster.ac.uk)

Key Points:

- 2014 Hubble Space Telescope imagery of Saturn's northern FUV auroras provides updated picture of statistical boundary locations
- Modulation of auroral intensity by rotating current systems was clearest at dawn local times during the north-south system coalescence
- This questions the idea that auroral and SKR emission enhancements simply track the rotating current systems

This article has been accepted for publication and undergone full peer review but has not been through the copyediting, typesetting, pagination and proofreading process which may lead to differences between this version and the Version of Record. Please cite this article as doi: 10.1029/2018JA025426

Abstract

The Hubble Space Telescope imaged Saturn's northern ultraviolet auroras during February–June 2014, when Saturn's northern and southern magnetic perturbation fields were locked in anti-phase and matched in rotation period (~ 10.69 h). During this coalescence period, we test for evidence of rotational modulation of the auroras using the latest rotating current system model and kilometric radio phases derived from Cassini measurements. While we see modulation of auroral intensity in the rotating frames of the planetary period current systems, the pattern is opposite to that expected and is dominated by an asymmetric local time profile that peaks at dawn. Enhancement of the north emission by rotating upward field aligned currents (FACs) is expected to peak at magnetic longitudes of $\sim 90^\circ$, whereas here the intensity increased at $\sim 270^\circ$. This unexpected finding is attributed to the presence of non-PPO dynamics having affected the auroral morphology, together with insufficient sampling of the rotational system orientations provided during such HST campaigns. Rotational modulation is clearest at dawn regardless of the pattern's orientation, suggesting that the physical relationship between rotating FACs and auroral intensity is not direct, having a local time dependence that is not generally observed in the rotating FAC magnitudes. We also find no statistically significant planetary period oscillation of the auroral circle position, but the mean centre was offset from the spin pole by $\sim 3^\circ$ latitude toward early morning local times. Mean auroral boundaries were located at equatorward and poleward colatitudes of $15.0 \pm 2.8^\circ$ and $12.4 \pm 3.0^\circ$.

1 Introduction

The field-aligned currents (FACs) that drive Saturn's main auroral emissions are thought to be associated with flow shears in the outer regions of the magnetosphere, as the magnetic field and plasma slow down from corotation with the planet in the inner magnetosphere and are influenced by the anti-sunward flow of the solar wind (e.g. Cowley et al., 2004a, 2004b; 2008; Bunce et al., 2008; Belenkaya et al., 2014; Hunt et al., 2015a). Extensive analyses of in-situ FAC signatures detected by Cassini have shown that the effective Pedersen conductivity of the ionosphere determines the latitude where these FACs maximize, and that the main upward current region is positioned slightly equatorward of the open-closed field line boundary (Hunt et al., 2015a,b). Upward FAC is carried by electrons travelling downward into the ionosphere, and so is important in generating auroral emissions. Note this sub-corotation or 'flow-shear' driven current system is different from the corotation enforcement currents that drive Jupiter's main auroral emissions (e.g. Vasyliunas, 1983); such currents at Saturn have been shown to be too weak to produce the observed main UV emission (Cowley & Bunce, 2003), and are not readily observed in magnetic signatures (Hunt et al., 2015b). To a first approximation, Saturn's steady-state auroral morphology is formed of a partial ring of emission, typically brighter on the dawn side of the oval than at dusk (e.g. Grodent et al., 2005; Lamy et al., 2009; Badman et al., 2011; Carbary, 2012). The center point of the oval is offset from the spin axis towards the nightside and dawn flank (e.g. Carbary, 2012; Nichols et al., 2016), the combined effect of solar wind flow upon the outer magnetosphere, and outflow of internally produced plasma down the dusk-side tail via the Vasyliunas cycle (e.g. Cowley et al., 2004a).

Observations from the Hubble Space Telescope (HST), Voyager and Cassini missions have also revealed a multitude of transient auroral features, related to both solar wind interaction and internal plasma processes, which modify the global auroral morphology. Rapid

intensification and poleward expansion of the dawn-side emission occurs during storm events, when solar wind compressions lead to reconnection in the tail (e.g. Prangé et al., 2004; Cowley et al., 2005; Grodent et al., 2005; Clarke et al., 2009; Meredith et al., 2015; Nichols et al., 2014). Patches or bifurcations separating from the dayside main emission signify reconnection at the magnetopause boundary with the Interplanetary Magnetic Field (IMF) (e.g. Radioti et al., 2011; Badman et al., 2013; Meredith et al., 2014; Kinrade et al., 2017). Small-scale, sub-corotating patches within the main emission are associated with instability mechanisms or resonances at the magnetopause (e.g. Masters et al., 2010; Grodent et al., 2011; Lamy et al., 2013; Meredith et al., 2013; Yao et al., 2017), and a periodic 1-h pulsing of poleward-moving forms has also been observed (Mitchell et al., 2016). Internal plasma processes at Saturn produce two main types of transient auroral signature. The first is associated with nightside reconnection following cyclic plasmoid release down the magnetotail. Dipolarization in the current sheet produces an auroral spot or expansion poleward of the main emission on the nightside, which then tracks equatorward and intensifies as it rotates around the dawn flank as the source region of hot plasma return flow travels sunward and inward through the outer magnetosphere (e.g. Mitchell et al., 2009; Jackman et al., 2013; Lamy et al., 2013; Mitchell et al., 2015). The second type is related to radial interchange of hot and cold plasma closer to the planet. These auroral signatures appear equatorward of the main oval, and have been observed following intense plasma injections from the magnetotail (Mitchell et al., 2009; 2015) and over longer timescales associated with centrifugally-driven interchange that has no local time preference (e.g. André et al., 2005; Hill et al., 2005; Radioti et al., 2013; Mitchell et al., 2015).

In addition to the flow-shear driven FACs and transient behaviors described above, Saturn's auroras and related radio emissions are also modulated by regions of FAC in each hemisphere that rotate with the planet at close to the planetary period. Planetary period oscillations (PPOs) permeate most measurements made within Saturn's magnetosphere (see review by Carbary & Mitchell, (2013) and references therein). Magnetic perturbation fields that rotate mostly independently in each hemisphere are thought to be responsible, producing regions of rotating current that link the high-latitude ionosphere and equatorial magnetosphere (e.g. Andrews et al., 2010; 2011). Important to this study, these rotating currents map closely to Saturn's main auroral emission region, and can have similar magnitude to the Sun-fixed current system that drives the main auroral emission (Hunt et al., 2015a,b; 2016). We therefore expect some level of modulation of Saturn's auroral intensity by rotating PPO FACs as they move through different local times.

Auroral emission at Saturn is physically linked with the production of Saturn kilometric radiation (SKR), a radio emission produced by acceleration of electrons along field lines that map down to the auroral oval (e.g. Lamy et al., 2008; Lamy et al., 2009; Lamy et al., 2010). First detected by the Voyager spacecraft (Kaiser et al., 1980), SKR emissions exhibit strong planetary period signals. SKR periodicity was attributed to a strobe-like emission source in the dawn sector of each hemisphere (e.g. Kaiser & Desch, 1982; Galopeau et al., 1995; Lamy et al., 2009), but is now thought to result from a rotating source region that intensifies at dawn (Andrews et al., 2011; Lamy, 2011; Lamy et al., 2013) where Saturn's auroral emission is also generally brightest (e.g. Gérard et al., 2004; Grodent et al., 2005; Nichols et al., 2016). Rotational modulation of Saturn's auroras with SKR period has been observed most clearly in the dawn sector of each hemisphere, with total UV power varying diurnally by a factor ~ 3 , maximising at peak SKR power (Nichols et al., 2010a). The nature of this modulation is also likely to vary over time, however, as indicated by periods of observed hemispheric asymmetry in the UV auroral response (Carbary et al., 2013; Nichols et al., 2016) and

possible interhemispheric modulation observed in the infrared auroral emission (e.g. Badman et al., 2012).

Although rotational modulation of the auroral intensity has been observed previously (e.g. Sandel et al., 1982; Nichols et al., 2010a), it is not always consistent with the regions of current flow expected from the present magnetic field-derived PPO current system model (described in Section 3). Badman et al. (2012) found that infrared auroral emissions recorded by the Cassini/VIMS between 2006-09 exhibited rotational modulation in both hemispheres, with the northern intensity showing an anti-phase dependence on the southern rotating current system, indicating possible interhemispheric coupling via PPO currents. Carbary (2013), analyzing Cassini UVIS auroral imagery recorded during 2007-09, revealed rotational modulation of both the intensity and latitudinal position (by several degrees) of the southern auroras, but saw no evidence of rotational modulation in the northern emissions. Nichols et al. (2016) analyzed northern hemisphere FUV auroral imagery from the HST throughout 2011-2013. Rotational modulation was present but varied for different campaign years, showing broad agreement with the PPO current system model in 2011-12, but was more consistent with interhemispheric modulation by the southern PPO current system in 2013.

The PPO systems also modulate the location of auroral emissions. Periodic tilting of the entire oval position has been observed in the southern hemisphere (Nichols et al., 2008; 2010b; Provan et al., 2009; Carbary et al., 2013; Bunce et al., 2014; Hunt et al., 2015a; Arridge et al., 2016) and in the north (Badman et al., 2016; Nichols et al., 2016). This oscillation has a near-planetary period, is elliptical in shape being aligned along a pre-midnight/pre-noon axis, and is offset from the spin pole by several degrees towards the midnight-dawn LT sector. The relative phasing of the oval displacement (dawnward and duskward shift) in each hemisphere, observed during the equinoctial HST campaign in 2009 (Nichols et al., 2009), indicated that oval oscillation is driven by the external magnetic perturbation fields – rotating independently in each hemisphere – and not the result of a magnetic axial offset (Nichols et al., 2010b).

Here we report observations of Saturn's northern FUV auroras made by the HST throughout February-June 2014, when the PPO systems in each hemisphere had converged to a common rotation period of ~ 10.69 h, and were locked in relative anti-phase (i.e. their effective dipoles were facing opposite directions) (Provan et al., 2016). This is an interesting interval of atypical PPO behavior, as the system configuration was expected to suppress interhemispheric coupling via FACs closing in the conjugate ionosphere. Evidence of interhemispheric PPO has been seen previously in SKR emissions (e.g. Lamy et al., 2011), auroral imagery (e.g. Badman 2016; Nichols et al., 2016) and magnetic signatures of FACs (Hunt et al., 2015b). We investigate the possible modulation of Saturn's northern auroral emission intensity by the rotating current systems, and compare with the analysis of 2011-13 HST images reported by Nichols et al. (2016). We also test the relationship between auroral intensity with SKR phase, which is derived independently from the magnetic PPO phase.

2 The HST 2014 campaign

This study analyzes 60 images of Saturn's northern FUV aurora captured by the HST Space Telescope Imaging Spectrograph (STIS) during 1 February - 14 June 2014. During this period Saturn was continuing to emerge from equinox into its northern spring season, with a sub-Earth latitude of $\sim 22^\circ$ allowing the HST to observe auroral emissions close to the

northern limb. Observations were made throughout 15 orbits on 1 February, 7 April, 10 April, 12-13 April, 25 May and 14 June. 30 out of 60 images were captured using the STIS FUV Multi-Anode Microchannel Array (FUV-MAMA) detector in 'clear' mode (F25MAMA), which detects emissions of wavelength 115-170 nm. The other 30 images were obtained using the F25SrF2 long-pass filter in time-tag mode, which excludes H Lyman- α emission at 121.6 nm, but passes the H₂ Lyman and Werner bands in the range ~125–190 nm. The STIS MAMA detector has 1024×1024 pixels, with a single pixel dimension of 0.025 arc sec. This translates to a range of distances subtended by a single pixel projected on the planet surface, but at nadir this is ~476 km with an Earth-Saturn distance of 8.2 AU (and taking account of the ~0.08 arc sec point spread function). Photon count rates were converted to intensity values of total unabsorbed H₂ emission across the wavelength range 70–180 nm, using conversion factors of 1 kR = 3994 (SrF2-mode) and 1072 (clear-mode) counts per second (Gustin et al., 2012) and assuming a color ratio of 1.1 across the auroral region. Individual exposure times varied between ~270 s for clear mode images, to 700-840 s for F25SrF2 filtered images. The latter exposure times reflect the need to improve the signal-to-noise ratio during a campaign in which Earth's geocorona was particularly bright. Together the images constitute ~21.8 h of cumulative exposure over the campaign. The full set of images is provided in the Supporting Information.

Image processing followed the pipeline steps developed by Boston University (Clarke et al., 2009; Nichols et al., 2009), including flat-fielding, dark count subtraction and geometric distortion correction. Planetary disk and geocoronal emissions were also removed using the method described by Clarke et al. (2009), i.e. determining best-fit Minnaert coefficients for the center-to-limb variation and using a latitudinal intensity profile extrapolated over the auroral region. At auroral latitudes the uncertainty in the empirically derived background is ~2–3 kR. The images were scaled to a standard distance between HST and Saturn of 8.2 AU and projected onto a 0.25° × 0.25° planetocentric latitude-longitude grid at an emission altitude of 1100 km above the 1 bar pressure level (Gérard et al., 2009). Spatial uncertainties in the images arise from determination of the planet center and distortion of projected pixels near the limb. Grodent et al. (2005) showed that this spatial uncertainty is ~1° for typical observation geometries (~1000 km on the planet surface). We have cropped the projected images to reduce the impact of distorted pixels on auroral boundary detections at local times between ~22-02 LT (around midnight), using a viewing angle limit of 83° (the planetary limb being at 90° i.e. a vector on the surface of the planet normal to the HST viewing direction).

3 Saturn's rotating current systems

Following detections from the Pioneer and Voyager missions, extensive analyses of SKR and magnetic measurements made by Cassini have revealed that Saturn exhibits two distinct rotation periods, one in the northern hemisphere and one in the southern (e.g. Kurth et al., 2008; Gurnett et al., 2009; 2010; Andrews et al., 2010; Espinosa & Dougherty, 2000; Lamy et al., 2011; 2017; Southwood, 2011; Fischer et al., 2015; Cowley et al., 2016). These two periodic signals have been detected in isolation within the respective polar cap regions, but have also been observed to superpose in the equatorial region, producing a variable beat period (Provan et al., 2011; 2012; Andrews et al., 2012; Hunt et al., 2015b; Cowley et al., 2016). The northern and southern periods and their respective amplitudes change over time, as catalogued principally in the work of Andrews et al. (2010; 2012) and Provan et al. (2014; 2016) throughout the lifetime of the Cassini mission, whereby a phase-tracking method is applied to the extracted PPO component of magnetic measurements over a ~100-200 day

sliding window. Short-term variations in PPO signal amplitude and phase have also been observed in both SKR and magnetic data, attributed to changes in the solar wind speed (e.g. Zarka et al., 2007) or pressure resulting in large-scale changes in the size of the magnetosphere (Provan et al., 2015).

The expected PPO FACs are, to a first approximation, directed downward into the ionosphere on one side of the polar region, flow as Pedersen current across the pole, and then upward and out of the ionosphere on the opposite side of the polar region before partially closing in the equatorial plane of the outer magnetosphere (e.g. Provan et al., 2009a; Andrews et al., 2010; Hunt et al., 2015b). At high latitudes these PPO FACs produce magnetic perturbation fields that have the approximated form of planet-centered dipoles, orientated perpendicular to the planetary field dipole, which rotate about the planetary spin axis in each hemisphere in the corotation direction. The perturbation field loops over the pole and down to the equatorial plane where the field is quasi-uniform and aligned with the effective dipole. For brevity we do not include circuit diagrams here, but direct the reader to the comprehensive description and diagrams of Hunt et al. (2015b). Azimuthal orientation of the PPO system in each hemisphere is defined using the angle of the effective equatorial dipole field direction from local noon, $\Phi_{N,S}$, proceeding anticlockwise (in the direction of planetary rotation), and is referred to as dipole angle or PPO phase. In this study we use PPO phase values from the empirical model of Provan et al. (2016), which provide an estimate of $\Phi_{N,S}$ for a given time (the central HST exposure time in this case).

To locate an auroral feature azimuthally in the rotating frame of the PPO system, a magnetic longitude system is defined, referenced to the model PPO system's effective dipole position at a particular time. By convention an auroral feature at azimuth ϕ (increasing anticlockwise from 0° at noon) has a magnetic longitude of $\Psi_{N,S}$, the clockwise angle from the PPO model dipole direction at phase $\Phi_{N,S}$ i.e. $\Psi_{N,S}(\phi, t) = \Phi_{N,S}(t) - \phi$. This is illustrated in Figure 1, which shows an auroral feature at azimuth ϕ within the northern magnetic longitude frame, Ψ_N , at an arbitrary time and northern dipole phase, Φ_N , as viewed from above the northern hemisphere.

Before analyzing auroral imagery for evidence of rotational modulation, it is important to consider where the upward and downward PPO FAC regions are expected to maximize as the system rotates. Hunt et al. (2015a,b) showed that rotating regions of PPO FAC, identified by magnetic fluctuations during high inclination orbits over each hemisphere, exhibit comparable magnitude and latitude to the PPO-independent currents. From the initial perturbation field model of Andrews et al. (2010), and more recent high-latitude field data studies of Hunt et al. (2015a,b), the primary PPO-related upward FAC is thought to maximize at a magnetic longitude of $\Psi_N = 90^\circ$ with respect to the northern hemisphere, with maximum downward FAC at $\Psi_N = 270^\circ$. This is shown in Figure 1 by the dot and cross, respectively. Conversely the southern hemisphere primary PPO system has maximum upward FAC at $\Psi_S = 270^\circ$ and maximum downward FAC at $\Psi_S = 90^\circ$. Consideration of the perturbation fields using Ampère's law indicates that the expected azimuthal modulation pattern by PPO FACs in each hemisphere varies with magnetic longitude, to a first approximation, as $-\sin \Psi_{N,S}$ poleward of the PPO FACs, and $+\sin \Psi_{N,S}$ across the auroral current sheet at higher colatitudes (e.g. Hunt et al., 2015b). Previous auroral observations have shown this modulation profile in the rotating frame to be more complex than a simple sinusoid, particularly in the northern hemisphere (e.g. Badman et al., 2012; Carbary et al., 2013;

Nichols et al., 2016), but it is this symmetry in the modulation pattern that we test for in this auroral imagery study.

We may also expect some level of modulation from rotating regions of interhemispheric FAC (as proposed by Southwood and Kivelson, 2007), having been observed to map from the southern into the northern hemisphere with magnitude and co-latitude comparable to the primary PPO and PPO-independent FACs (Hunt et al., 2015b). The primary and interhemispheric FACs flow on the same magnetic field lines, and it is the net current flow that we expect to modulate the auroras. During the coalescence period of the PPOs, the primary upward and downward currents in each hemisphere were expected to flow at the same local time sector, i.e. the northern and southern current systems are expected to cancel each other to some extent between hemispheres through closure in the equatorial plane (see Provan et al., 2016, Figure 10). But with the north and south PPO systems locked in near anti-phase, and their relative FAC strengths unknown (see note about amplitude ratios below), it is difficult to decouple their auroral modulation effects from each other. Nevertheless the systems were not in perfect anti-phase, and we also test for auroral manifestation of southern PPO modulation in Section 4.

The rotational behavior has also been described using phase systems based on the periodic SKR emission peaking in the post-dawn sector (e.g. Desch and Kaiser, 1981; Kurth et al., 2007; 2008; Lamy 2011). During the coalescence interval of interest, the periods of the magnetic field oscillations (described above) were found to be the same as those derived from the SKR bursts, however the two systems were out of phase by 90-180° (Provan et al., 2016). This phase difference indicated that the northern SKR emission maximized when the northern effective dipole was pointed post-dusk, therefore the inferred maximum upward currents were located post-noon. The dominant SKR sources were correspondingly inferred to be located post-noon (this is discussed further in Section 4.4).

Provan et al. (2016) provide the amplitude ratio, k , of the northern and southern system oscillations, based on near-equatorial measurements of the phase modulations caused by the two signals superposing in this region. This is a measure of the relative strength of the north and south magnetic perturbation fields, and therefore a proxy for the relative magnitude of the associated FACs flowing at high latitudes. The amplitude ratio was not determined during this observation period due to orbit limitations, however values from highly inclined orbits between late 2012-early 2013, $k \sim 1$, and equatorial orbits between early-late 2015, $k \sim 2.3$, indicate that the systems were either of similar strength or north-dominated during these intervals.

4 Auroral observations

4.1 Global morphology

Here we update the developing picture of Saturn's global auroral morphology with 2014 observations, finding the mean distribution of emission intensity in local time, together with statistical colatitudinal boundaries (Section 4.2). The extraction of auroral boundaries is intended for comparison with Nichols et al. (2016), who analyzed images of Saturn's auroras from HST campaigns between 2011-13.

All 60 images were first rotated into a fixed local time (LT) frame, resulting in a planetocentric longitude-latitude grid of 1440×720 pixels respectively. Averaging of emission

intensity (in kR) was then performed on each individual pixel by summing through the images and dividing by the number of pixel counts. Figure 2 shows the resulting average emission intensity in 2014, shown in stereographic projection and contoured for levels of brightness between 0-20 kR. Intensity levels < 0 kR result from over-estimation of the planetary disk emission removal (see Section 2), as shown by the dark gray areas. Intensity levels > 20 kR are shown in orange to highlight the brightest areas of emission. The white area at the top of the figure shows the region beyond the planetary limb from the HST position, which has been cropped to remove distorted pixels in the projection. Although this average picture encompasses all of the auroral variability throughout the campaign, it does not reflect continuous observation of auroral activity at Saturn. The complete set of campaign images is provided in Supplementary Information S1.

The overall emission morphology is similar to previous analyses and formed of several main features. A clear dawn arc region extends through morning local times of ~ 3 -9 LT, with mean intensities > 20 kR peaking between ~ 05 -06 LT. The dawn arc displays a colatitude range of ~ 12 - 17° , shifting further poleward with later local time (we further define colatitude boundaries in section 4.2). Another active region of the morphology is located between ~ 11 -13 LT and ~ 7 - 15° colatitude (with 4-8 kR mean intensity levels), and is likely attributable to the presence of dayside magnetic reconnection signatures poleward of the main emission (e.g. Meredith et al., 2014; Nichols et al., 2016; Kinrade et al., 2017). Between ~ 13 -21 LT (up to the cropped edge of the image) the emission extent broadens to between ~ 7 - 25° colatitude, and exhibits a near-uniform low-level brightness of between 0-4 kR. A more active area within this dusk emission (4-8 kR) is evident beyond 18 LT between ~ 10 - 18° colatitude.

Variability of the dusk-side emission has been linked with a number of magnetospheric processes, including plasmoid ejections and subsequent magnetotail reconnection (e.g. Jackman et al., 2013), rotating signatures of dayside magnetopause reconnection (Radioti et al., 2011; Badman et al., 2013), radial interchange instabilities (e.g. Mitchell et al., 2009) and scattering of electrons into the ionosphere causing diffuse aurora (Grodent et al., 2010).

4.2 Boundary locations

Quantifying the variation of auroral emission boundaries is important for understanding the driving processes in the magnetosphere and how they map to the ionosphere at different local times. We identified main emission boundaries using the method employed by Nichols et al. (2016), whereby Gaussians are fitted to latitudinal profiles of intensity averaged over 10° of longitude (equivalent to 40 min local time). The poleward and equatorward boundaries are then taken at the respective latitudinal intersects of the Gaussian full width half maximum (FWHM). At times in 2014, the northern main auroral emission was observed to disappear almost entirely for several hours (Kinrade et al., 2017). To ensure that only distinct bands of emission were included in the boundary statistics, intensity profiles having maximum values < 10 kR or poor Gaussian fit suitability (based on χ^2 testing) were rejected. Boundaries were not detected on the nightside, because the main emission lay beyond or close to the planetary limb from the HST's perspective. Figure 3 shows the detected auroral boundaries from all images plotted in polar projection and fixed in LT. Blue and red dots mark poleward and equatorward boundaries detected within each local time bin respectively. Solid lines show the mean poleward (blue) and equatorward (red) emission extents, based on the boundary dots.

The grey shaded area represents the $1-\sigma$ 'envelope' encompassed by the standard deviation of poleward and equatorward boundary latitudes in each LT bin. Also plotted are the mean poleward (yellow line) and equatorward (green line) northern emission boundaries observed during HST imaging campaigns throughout 2011-13, as reported by Nichols et al. (2016).

Mean co-latitude boundaries ($\theta_{\text{eq,pl}}$) and standard deviations ($\sigma_{\text{eq,pl}}$) for each LT bin are listed in Table 1.

The steady-state dawn arc morphology is clear in Figure 3a. Referring also to Table 1, the mean auroral boundaries between 0300-0900 LT have standard deviation of $\sim\pm 1^\circ$ colatitude (see gray-shaded values in Table 1). The mean equatorward (poleward) boundary was located at $18.8\pm 0.9^\circ$ ($15.3\pm 1.0^\circ$) colatitude at 0300 LT, reducing to $14.8\pm 0.8^\circ$ ($12.8\pm 1.1^\circ$) at 0900 LT. The mean position of the dawn arc thus shifted poleward with later LT (the equatorward boundary by at least several degrees). The latitudinal extents of the dawn arc in 2014 are formally consistent with the Nichols et al. (2016) observations during 2011-13. Consider the 0620 LT bin, for example, within which the 2014 mean equatorward (poleward) boundary was located at $15.7\pm 0.9^\circ$ ($13.9\pm 1.0^\circ$) colatitude compared to $15.8\pm 1.1^\circ$ ($13.4\pm 2.1^\circ$) derived during 2011-13. Note the extended nightside image coverage in 2014 as a result of Saturn having progressed further into its seasonal northern spring.

At local times later than ~ 0900 LT, the 2014 mean emission boundaries moved further poleward and displayed more variation in latitude (note the general broadening of the $1-\sigma$ shaded area in Figure 3a). A poleward ‘shift’ in the morphology is evident between 0900-1100 LT, with the mean equatorward (poleward) boundary colatitude reducing from $14.8\pm 0.8^\circ$ ($12.8\pm 1.1^\circ$) to $11.3\pm 1.2^\circ$ ($7.9\pm 1.6^\circ$). Nichols et al. (2016) also observed this pre-noon, local time boundary in HST images from 2011-13, citing the presence of poleward auroral forms around noon to be the probable cause. Poleward forms around noon were also present during this 2014 campaign (Kinrade et al., 2017), and were identified as signatures of dayside reconnection processes. Auroral features poleward of the dayside main emission have been previously linked with cusp emission and ‘bursty’ reconnection during periods of magnetospheric compression by the solar wind (e.g. Gérard et al., 2005; Radioti et al., 2011; Badman et al., 2013; Meredith et al., 2015), although reconnection signatures in the dayside aurora have also been observed during quiet solar wind conditions, and in absence of any other main emission morphology (Kinrade et al., 2017).

Figure 3b is a normalised histogram showing the distribution of equatorward (red) and poleward (blue) auroral boundary colatitudes, calculated using all the detected boundary points in Figure 3a. Bins are 0.5° wide, and transparency has been used in bins where equatorward and poleward distributions overlap. The horizontal coloured bars above the distributions show the respective overall mean colatitude (solid vertical line) and $1-\sigma$ standard deviation around the mean (shaded horizontal bar). Corresponding means from Nichols et al. (2016) for 2011-13 equatorward (green) and poleward (yellow) boundaries are also plotted, and show general agreement. The 2014 overall equatorward (poleward) boundary colatitude of $15.0\pm 2.8^\circ$ ($12.4\pm 3.0^\circ$) is formally consistent with the Nichols et al. (2016) value of $14.6\pm 2.3^\circ$ ($10.3\pm 3.8^\circ$). Carbary et al. (2012), who performed a statistical analysis on 180.3 h of cumulative northern UV imagery from Cassini UVIS, found a maximum intensity boundary of $15.1\pm 1.0^\circ$, in broad agreement with the colatitude extents here. Reflecting the aforementioned post-noon boundaries shown in Figure 3a, the 2014 colatitude distributions exhibit a poleward skew, showing similarity with the (perhaps under-sampled here) bimodality also observed by Carbary et al. [2012] and Nichols et al. (2016).

In summary, the 2014 northern auroral morphology was broadly consistent with previous observations in 2011-13. The average dawn arc region, where emissions occur within a

narrow latitudinal band between ~0300-0900 LT, is distinct from the more variable and poleward-shifted emissions within the pre-noon and noon-dusk sectors.

4.3 Rotational modulation of emission intensity

We tested the auroral images for evidence of rotational modulation of the emission intensity associated with PPO current systems. There are two separate questions to answer: does the emission brighten or dim at certain magnetic longitudes (i.e. within the rotating PPO frame), and does this ordering vary with PPO dipole direction (i.e. with respect to the PPO system orientation in local time)?

Images were each rotated into a fixed magnetic longitude (Ψ) frame, using the central exposure time (UT) and corresponding model PPO dipole phase (Φ) from Provan et al. (2016). Figure 4 shows the mean northern emission morphology in fixed magnetic longitude for the northern (4a) and southern (4b) PPO systems, obtained by averaging the intensity of each pixel location within each of the magnetic longitude-fixed images. Starting with the northern magnetic longitude frame in Figure 4a, the intensity maximizes along a wide range of longitudes between $\Psi_N = \sim 165\text{-}325^\circ$ (taking the light blue 3-6 kR contour as a visual threshold), as a latitudinal band of 2-4° around the typical main emission location at $\sim 15^\circ$ colatitude. This region of higher intensity is distinct from the unexpected and mostly continuous band of low intensity (0-3 kR) between $\sim 10\text{-}20^\circ$ colatitude at all magnetic longitudes, which we interpret as contribution from emissions not ordered by magnetic longitude (being driven by the PPO-independent current system fixed in local time, for example). The magnetic longitude sector in which the intensity maximizes, between $\Psi_N = \sim 165\text{-}325^\circ$, is almost opposite to where the PPO system model predicts the maximum upward current to be around $\Psi_N = 90^\circ$. Similar ordering of the northern intensity is also evident in the southern magnetic longitude frame (Figure 5b), except the intensity maximized between $\Psi_S = \sim 330\text{-}125^\circ$ i.e. a sector opposite to where the intensity maximized in the northern magnetic longitude frame (compare Figures 4a and 4b). This is expected given that the northern and southern PPO systems were locked in near anti-phase with a common period of ~ 10.69 h during early 2014 (see Section 3). The apparently stronger amplitude of the rotational modulation by the southern system compared to the north is surprising (compare the orange shaded-areas in Figure 4a and 4b), as, during the coalescence period (see Section 3), the primary region of rotating upward current around $\Psi_N = 90^\circ$ in the northern hemisphere is typically expected to be of equal or larger magnitude than the interhemispheric current closing from the southern hemisphere at $\Psi_S = 90^\circ$.

To isolate any rotational modulation of intensity from the PPO-independent local time profile, we examined the northern images as a function of PPO phase, $\Phi_{N,S}$. First the intensities were averaged over 1 h LT bins, and then the maximum between 0-20° colatitude was found in each LT sector. These maximum intensities were then binned according to the PPO phase angle of each image, and averaged using five phase space bins of 72° ranging from $\Phi_{N,S} = -180\text{-}180^\circ$, resulting in the coloured spectrograms of Figure 5, which show the intensity versus PPO phase for the northern (5a) and southern (5b) rotating current systems. Two cycles of PPO phase have been plotted vertically to clarify any periodicity in the LT or intensity variation. Diagonal lines of constant $\Psi_{N,S} = 90^\circ$ (white dashed) mark the magnetic longitude of maximum upward field aligned current expected for the respective PPO systems as they rotate through local time (remembering that the upward FAC closure of the southern primary PPO current in the northern hemisphere is at $\Psi_S = 90^\circ$). Subpanels to the top and

right of Figures 5a and 5b show mean intensities in each LT and PPO phase bin respectively, with error bars indicating standard errors with respect to the number of images in each bin.

The mean LT variability of the northern intensity is clear from the top subpanels in Figure 5 (identical by definition in 5a and 5b), with a peak of ~ 30 kR at dawn between 05-06 LT, and a minimum of ~ 5 kR around midnight between 22-02 LT. Interestingly, secondary peaks are visible at dusk around 18-19 LT (~ 13 kR), and around noon between 11-15 LT (~ 11 kR). The local time variability here is consistent with the average fixed LT morphology shown in Figure 2.

The spectrogram in Figure 5a shows that the northern intensity did not maximize at any constant PPO phase, but was dominated by a strong LT profile being generally higher at dawn. Variation of the dawn-side intensity with Φ_N is clearest in the 05-06 LT bin, for example, peaking between PPO phases $\Phi_N = 108-180^\circ$ and reducing at $\Phi_N = 252-324^\circ$. The overall intensity also peaked at 13.9 ± 1.0 kR between $\Phi_N = 108-180^\circ$, which is significantly out of phase with the model value of $\Phi_N = 0^\circ$ (see Section 3). The intensity did not appear to maximize at the expected northern magnetic longitude, shown by the dashed white line at $\Psi_N = 90^\circ$. Figure 5b shows that the northern intensity showed no strong dependence on specific southern PPO phases, displaying the same strong LT variation seen in Figure 5a. The dawn-side intensity did peak at the expected magnetic longitude for upward FAC associated with the southern PPO system closing in the north i.e. the southern PPO dipole at $\Phi_S = 0^\circ$, or equivalently $\Psi_S = 90^\circ$ at local dawn. As described for Figure 4, this is attributed to the two phase systems being approximately in anti-phase, i.e. a shift of the northern distribution. With enough observations and while the systems are not locked in anti-phase, this comparison may be a way of determining the relative amplitudes of the north and south PPO systems independently to the magnetically derived amplitude ratio, k .

The HST can of course only observe Saturn at certain times, and so there exists an observation bias in the PPO dipole phases that we sample. Using relatively wide PPO phase bins of 72° provided an image distribution of 9, 15, 15, 8 and 13 images in bins ranging through $-180-180^\circ$, respectively. To reduce the effect of any PPO phase sampling bias, the intensity as a function of magnetic longitude (Ψ) may also be calculated i.e. the intensity variation within the rotating reference frame of the PPO system, referenced only to the direction of the effective dipole (see Section 3 and Figure 1). Figure 4 shows the mean auroral spatial morphology in this way, but here we bin the maximum intensity in LT and magnetic longitude to directly compare with the sinusoidal modulation pattern anticipated from rotating PPO FACs. Figure 6 shows colored spectrograms for the maximum intensity sorted by 1 h LT and 72° magnetic longitude bins. Two complete cycles of magnetic longitude are plotted to highlight any periodicity. Right panels show the mean-maximum intensity in each longitude bin (black line, with standard error bars). Red sinusoids show the expected longitudinal modulation pattern in the northern hemisphere from the northern primary (6a) and southern interhemispheric upward FACs (6b), peaking at $\Psi_{N,S} = 90^\circ$ respectively, scaled in each case to the peak-to-peak overall intensity.

Any significant ordering of emission intensity within the magnetic longitude system would be evident in Figure 6 as horizontal bands of colour. Figure 6a shows no consistent intensity banding across the range of local times, indicating an absence of purely rotational modulation of the auroras by primary rotating FACs during this period. However, more subtle intensity variation with longitude at each local time is visible on top of the local time variation profiled

in Figure 5, particularly in the morning sector. This weak rotational modulation with Ψ_N is apparent in the global mean intensity, with periodicity clear in the right panel of Figure 6a. Global intensity peaked between $\Psi_N = 252\text{-}324^\circ$ and was lowest between $\Psi_N = 108\text{-}180^\circ$, with a peak-to-peak factor of ~ 2 . Compared with the red sinusoid trace, the observed modulation pattern is almost 180° out of phase with the model expectation; a finding already indicated by the rotating-frame-fixed morphology shown in Figure 4.

Figure 6b shows similar modulation of the northern intensity with southern magnetic longitudes, the distribution again being dominated by a clear LT variation. The overall intensity response peaked between $\Psi_S = 108\text{-}180^\circ$ and was lowest between $-36\text{-}36^\circ$ (around $\Psi_S = 0^\circ$). This intensity variation with southern magnetic longitude is close to the expected interhemispheric modulation pattern (being only slightly offset from the red sinusoid). The near anti-phase relationship between the north and south PPO systems during coalescence means, however, that any observed modulation cannot be separated into primary and interhemispheric current effects, as the rotating FACs flow on the same magnetic field lines. Again, the modulation pattern observed in Figure 6b is largely a $\sim 180^\circ$ longitude-shifted version of that in Figure 6a, consistent with the spatial intensity distribution of Figure 4b.

We also tested for planetary period oscillation of the position of the auroral oval using a circle fitting method described by Nichols et al. (2016) and detailed in Appendix A. We found that the average auroral circle was displaced by an average $\sim 3^\circ$ toward 02 LT, but no statistically significant oscillation of its position with north magnetic PPO phase was observed.

4.4 Modulation with SKR phase

Here we make an additional test for rotational modulation of the auroral intensity in early 2014 using the SKR phase, independent of the PPO current system model.

Figure 7 is a histogram of maximum auroral intensity across all 1-hr LT bins (as described in Section 4.3) versus northern SKR phase, Φ_{NSKR} , derived empirically from Cassini RPWS measurements (Lamy et al., 2011). SKR phase bins are 72° wide to match the magnetic PPO phase histograms shown in Figure 5. Vertical error bars indicate the standard deviation about the maximum intensity in each phase bin. The auroral intensity was brightest in the $-36^\circ < \Phi_{\text{NSKR}} < 36^\circ$ bin i.e. around $\Phi_{\text{NSKR}} = 0^\circ$.

We note that the derived SKR phase is dependent on the viewing angle of Cassini in relation to the nearest peak SKR emission source – secondary SKR emission sources have been observed around dusk and midnight (Lamy et al., 2009). Based on past observations of peak SKR emission power, the total northern auroral intensity is expected to maximize at $\Phi_N = 0^\circ$ and $\Phi_{\text{NSKR}} = 0^\circ$. In this orientation, the effective northern perturbation dipole, directed toward local noon, implies a maximum rotating upward FAC (around magnetic longitude $\Psi_N = 90^\circ$) passing through the dawn sector. In fact, during this interval of north-south coalescence, Provan et al. (2016) found that the SKR maximised at $\Phi_N = 90^\circ\text{-}180^\circ$, putting the maximum upward FAC of the model at 12-18 LT. Our results show that the UV intensity peaked at $\Phi_{\text{NSKR}} = 0^\circ$ (see Figure 7), but in the dawn sector (see Figure 5). To reconcile these findings we consider that if, at the time of peak SKR (i.e. $\Phi_{\text{NSKR}} = 0^\circ$), $\Phi_N = 90^\circ\text{-}180^\circ$, as found by Provan et al. (2016), the most intense dawn sources would be at magnetic

longitudes $\Psi_N = 180\text{-}270^\circ$ (see Figure 1). This is in agreement with the result shown in Figure 4a, where the intensity peaks through this longitude sector.

5 Discussion & summary

This study has examined 60 images of Saturn's northern FUV auroral emissions, captured by the HST STIS between February and June 2014 (provided in the Supporting Information S1). We updated the current picture of Saturn's global 'steady-state' auroral morphology with the mean spatial intensity distribution and latitudinal boundaries. Mean equatorward and poleward boundaries of $15.0 \pm 2.8^\circ$ and $12.4 \pm 3.0^\circ$ colatitude, respectively, are consistent with those from images in 2011-13 (Nichols et al., 2016). The dawn arc region, where emissions form a narrow latitudinal band between $\sim 0300\text{-}0900$ LT, continues to be morphologically distinct in position and intensity from the more variable and poleward-shifted emissions that develop between pre-noon and the dusk sector. Interestingly we also see a secondary UV emission peak around $\sim 1800\text{-}1900$ LT, which has been reported previously in northern infrared emissions (Badman et al. 2012), and in both SKR and UV emissions by Lamy et al. (2009), who suggested that the persistence of this feature may indicate the direct generation of accelerated electrons on the duskside.

We tested the auroral intensity and location for modulation by rotating FACs associated with the magnetic PPO system.

Figures 4a and 6a show that the mean northern intensity in early-mid 2014 was ordered in the rotating frame of northern magnetic longitude (i.e. not evenly distributed), but not in the way anticipated from the rotating current system model. Intensity maximized across a wide swathe of magnetic longitude $\Psi_N = \sim 252\text{-}324^\circ$ i.e. $\sim 180^\circ$ out of phase with the FAC model sinusoid peak at $\Psi_N = \sim 90^\circ$ for upward current in the northern hemisphere. This is consistent with Nichols et al. (2016) who reported intensity enhancement between $\Psi_N = \sim 200\text{-}340^\circ$ in 2011-2013 FUV imagery. We attempted to isolate local time effects from the rotational modulation. A clear asymmetry in the intensity-local time profile was dominant, with brightest auroras in the dawn sector by a factor $\sim 2\text{-}3$ compared to the dusk sector. The rotational modulation was clearest at dawn, but with sinusoidal response in magnetic longitude apparent when averaging intensities across all local times.

The mean northern intensity maximized between PPO phases of $\Phi_N = 108\text{-}180^\circ$, which is out of phase with the model value of $\Phi_N = 0^\circ$ derived from magnetic measurements. Badman et al. (2012) reported similar enhancement of the mean northern IR auroral intensity at $\Phi_N = 108\text{-}180^\circ$, based on 78 Cassini VIMS pre-equinox images during October 2006-February 2009. During April-May 2013, Nichols et al. (2016) found the FUV northern auroral intensity increased in the dawn sector for similar northern dipole phases of $\Phi_N = 90\text{-}180^\circ$ (one year prior to the 2014 campaign). This persistent auroral observational disparity with the PPO model is intriguing, because the perturbation field model continues to fit with independent, long-time SKR and magnetic FAC signatures measured by Cassini (e.g. Provan et al., 2016), which we expect to be closely associated with auroral emission production. As expected we found the total northern UV intensity in early 2014 to peak around an SKR phase of $\Phi_{\text{NSKR}} = 0^\circ$.

It is likely that non-PPO dynamics have affected the observed modulation pattern in this limited dataset, which we suggest may also be an important factor to consider in similar analyses. For example, 10 out of 60 2014 HST images show, atypically, absence of any dawn arc emission coincident at magnetic longitudes around $\Psi_N = 90^\circ$ (see annotated images in Supporting Information S1 and Kinrade et al., 2017). Conversely, a strong dawn arc persisting over 5 hours (12 consecutive images on the 12-13 April, see S1) was sampled at longitudes around $\Psi_N = 180\text{-}300^\circ$, an observation that has clearly affected the apparent modulation pattern here. Although rotational modulation is clearly influencing the overall auroral intensity (see Figure 6), the observed longitudinal dependence is sensitive to both the sampling distribution of PPO system orientations and any non-PPO or transient dynamics captured in the images.

The northern intensity pattern in the southern PPO rotating frame initially suggests possible interhemispheric modulation. Dawn sector emissions increased at southern PPO dipole angles about $\Phi_S = 0^\circ$, and the overall intensity was brightest between magnetic longitudes $\Psi_S = \sim 36\text{-}180^\circ$. Similar behaviour has been seen in pre-equinox northern infrared emissions (Badman et al., 2012), although typically we expect that any modulation from the primary rotating FAC system in the north will dominate over any interhemispheric current closure from the southern PPO system. As noted earlier, the amplitude of the northern and southern oscillations could not be determined at this time but the north was dominant both before and after (Provan et al., 2016). The anti-phase lock condition of the north and south PPO systems during their coalescence, however, means that effectively we are unable to separate northern from southern current system modulation, as the rotating FAC contributions from both systems flow on the same field lines, and it is the net current that we expect to modulate the aurora. The peak with southern longitudes is therefore essentially the northern distribution shifted by 180° .

Application of a circle fitting procedure to the HST images resulted in no clear evidence of northern oval oscillation with PPO phase in 2014 (see Appendix). A mean oval position offset of $\sim 3^\circ$ latitude towards ~ 02 LT was present, however, being broadly consistent with the focal point of oscillation reported previously by Nichols et al. (2016). An apparent absence of oval oscillation in 2014, following a statistically significant presence in 2013, suggests damping of the oscillation arising from some change in the PPO system behaviour; although circle-fitting was limited to 26 suitable images because of the mixed auroral morphology throughout the campaign.

Overall, our results indicate that while there was PPO modulation of the total UV auroral intensity during the PPO coalescence period, this was most evident at dawn local times (see Figures 5 & 6), suggesting the physical relationship between the rotating FACs and the UV intensity is not as straightforward as expected. The PPO-independent FAC has been observed to exhibit the same magnitude between midnight and pre-noon, plus we expect the PPO FACs to have largely the same magnitude as they rotate around all local time sectors (Hunt et al., 2016). Thus the dawn sector modulation observed here cannot be solely attributed to rotating FACs, suggesting the presence of a local time asymmetry in auroral source population or conductivity.

The uneven sampling distribution of PPO system orientations typical of time-limited HST observation campaigns requires careful consideration in similar future analyses. With the end of the Cassini mission, we now have no in-situ measure of Saturn's magnetic fields or SKR emission. It is important that we understand the relative merits and limitations of remotely-

sensed auroral imagery in tracking Saturn's rotational dynamics. An upcoming study will investigate all publicly available Cassini imagery of the ultraviolet auroras for evidence of PPO modulation.

6 Acknowledgements

This work is based on observations made with the NASA/ESA Hubble Space Telescope (observation ID: GO13396), obtained at the Space Telescope Science Institute (STScI), which is operated by AURA, Inc., for NASA. The Hubble observations are available from the MAST (<https://archive.stsci.edu/hst/>) or APIS (<https://apis.obspm.fr>) repositories, supported by the STScI (<http://www.stsci.edu/hst>). SKR phase data can be retrieved from publications and are also available from the webpage http://www.lesia.obspm.fr/kronos/skr_periodicity.php. All PPO phase data (2004-2017) are freely available on the University of Leicester Research Archive (<http://hdl.handle.net/2381/42436>). JK and SVB were supported by STFC grant ST/M001059/1. SVB was also supported by an STFC Ernest Rutherford Fellowship ST/M005534/1. GP and SWHC were supported by STFC Consolidated grant ST/N000749/1. LL was supported by CNES and CNRS/INSU programs of planetology and heliophysics.

7 Appendix A: Rotational modulation of auroral position

Saturn's auroral oval has been observed to oscillate by 1-2° in position with planetary period (Nichols et al., 2008; 2010b; 2016; Badman et al., 2016; Hunt et al., 2015a), and so we attempted to resolve this motion using 2014 HST imagery. The method of Nichols et al. (2008; 2016) relies on fitting circles to the individual auroral images (as a first approximation of the area extent of auroral emissions at Saturn), and monitoring the position of the circle centre-point as the PPO current system rotates. The systematic fitting of circles was limited to those images displaying clear equatorward emission boundaries (see Section 4.2) in both the dawn and dusk sectors to constrain the fit, however during the 2014 campaign only 26 images were found to be suitable. The auroral oval morphology was very mixed, including periods during which the dawn arc disappeared completely (Kinrade et al., 2017). We found no statistical oscillation of the oval position using these images, but the oval (when present) was offset by a mean ~3° towards a local time of ~02 LT, consistent with the offset reported by Carbary et al. (2012) and Nichols et al. (2016). We include the circle-fitting analysis here for completeness, together with a review of the oval oscillation behaviour described in previous studies.

The intermittency of auroral imaging campaigns at Saturn makes it difficult to constrain exactly how the oval displacement varies within the rotating magnetic phase systems. Nichols et al. (2010a) (using HST ACS imagery from the 2009 equinox campaign) reported a broad relationship with SKR phase in each hemisphere, finding that each oval was displaced duskward of the mean latitude position when the respective SKR phase was < 180°, and dawnward for SKR phases > 180°. Consideration of the effective PPO dipole directions derived from Cassini magnetic measurements (Provan et al., 2009b) led Nichols et al. (2010b) to suppose that the maximum equatorward offset of the oval occurred in the direction of the northern effective dipole in the north (at $\Psi_N = 0^\circ$), and opposite to the southern effective dipole in the south (at $\Psi_S = 180^\circ$). FAC signatures in Cassini magnetic measurements also showed that the location of the main auroral current sheet is modulated

with southern PPO phase (Hunt et al., 2015a), except with maximum equatorward displacement observed at $\Psi_S = 270^\circ$ i.e. near to where the upward PPO-related current maximizes. Badman et al. (2016) reported a case study that showed the northern auroral oval displaying similar oscillation in combined imagery from HST and Cassini i.e. tilting equatorward in the direction of maximum PPO-related current at $\Psi_N = 90^\circ$. Nichols et al. (2016) analyzed northern auroral images from HST campaigns in 2011, 2012 and 2013, and found statistical oscillation in both the noon-midnight and dawn-dusk directions with amplitudes of $\sim 0.5 \pm 0.3^\circ$ and $\sim 1.6 \pm 0.2^\circ$ latitude respectively. Tilting of the oval was found to be most equatorward at magnetic longitudes of $\Psi_N \sim 45 \pm 5^\circ$ e.g. a maximum duskward displacement to lower latitudes at $\Phi_N \sim 135 \pm 5^\circ$. This magnetic longitude ordering is again different to that proposed by Nichols et al. (2010b) (based on equinoctial auroral imagery from HST and using SKR phase) or that implied by the southern FAC observations of Hunt et al. (2015a), being midway between $\Psi_N = 0^\circ$ and $\Psi_N = 90^\circ$, respectively.

Circles were fitted to the mean equatorward auroral boundaries in each image (see Section 4.2). The circle center positions were then tracked in time and corresponding PPO dipole phase using the latest model values from Provan et al. (2016). Figure 8 shows the coordinates of the fitted circle center points (black crosses) versus northern PPO dipole phase, Φ_N ; x is along the midnight-noon axis and is positive toward noon (8a), and y is the dawn-dusk component, positive toward dusk (8b). Vertical error bars show the uncertainty in the circle fit, based on the sum-square mean distance of the boundary points from the circle. Best-fit sinusoidal functions of the form $f(\Phi_N) = \alpha \sin(\Phi_N - \Phi_0) + \beta$ are also plotted (black lines), the equations for which are shown in the top left of each figure panel. The associated dark grey shaded regions indicate the combined 1-sigma uncertainties in the amplitude (α) and vertical offset (β) fit parameters. Vertical dash lines mark the point of maximum anti-sunward (8a) and dusk-ward (8b) displacement, with the associated light grey region indicating the 1- σ uncertainty in the phase offset (Φ_0) parameter of the fit. Horizontal dash lines show the average oval offset position in x and y based on the best fit.

While the oval centre was generally offset from the spin pole by several degrees, the amplitude and errors associated with the sinusoid fits indicate that there was no observed relationship between oval displacement and northern PPO dipole phase i.e. the fit is consistent with a straight line. We reiterate that this statistical outcome is based on the limited sample set of 26 images, and the lack of dipole angles sampled between $\Phi_N \sim 230$ - 330° has contributed towards a significant error in the phase at maximum offset of $\sim \pm 78^\circ$ and $\pm 88^\circ$ for x and y components respectively. Nominally the phasing of the fit is such that maximum duskward offset (y component) occurred at around $\Phi_N \sim 180^\circ$, however the error range of the phase offset parameter is of the same order of longitude i.e. this fit is not statistically significant. Oscillation amplitudes for the noon-midnight (x) and dawn-dusk (y) components were $\sim 0.5 \pm 0.5^\circ$ and $\sim 0.3 \pm 0.4^\circ$ i.e. consistent with zero. The mean oval offset from the pole is characterised by the vertical offset fit parameters of $\beta_x = -2.6 \pm 0.4^\circ$ and $\beta_y = -1.3 \pm 0.3^\circ$ (horizontal dash lines in Figure 7), or a vector of $\sim 3^\circ$ from the spin pole in a local time direction of ~ 02 LT. Sinusoidal oscillation fits from Nichols et al. (2016) are also shown in Figure 7 by blue dot-dash lines (equations also labelled in blue). Comparing this with the 2014 crosses and sinusoid in Figure 8b, it's clear that the dawn-dusk oscillation amplitude of $\sim 1.6 \pm 0.4^\circ$ observed by Nichols et al. (2016) has not been resolved here. This is likely due in part to inadequate sampling, but could feasibly be attributed to some change or damping of the oval oscillation in response to the wider PPO climate as the northern and southern systems entered a period of coalescence (Provan et al., 2016).

8 References

André, N., M. K. Dougherty, C. T. Russell, J. S. Leisner, and K. K. Khurana (2005), Dynamics of the Saturnian inner magnetosphere: First inferences from the Cassini magnetometers about small-scale plasma transport in the magnetosphere, *Geophys. Res. Lett.*, 32, L14S06, doi:10.1029/2005GL022643.

Andrews, D. J., A. J. Coates, S. W. H. Cowley, M. K. Dougherty, L. Lamy, G. Provan, and P. Zarka (2010), Magnetospheric period oscillations at Saturn: Comparison of equatorial and high-latitude magnetic field periods with north and south Saturn kilometric radiation periods, *J. Geophys. Res.*, 115, A12252, doi:10.1029/2010JA015666.

Andrews, D. J., B. Cecconi, S. W. H. Cowley, M. K. Dougherty, L. Lamy, G. Provan, and P. Zarka (2011), Planetary period oscillations in Saturn's magnetosphere: Evidence in magnetic field phase data for rotational modulation of Saturn kilometric radiation emissions, *J. Geophys. Res.*, 116, A09206, doi:10.1029/2011JA016636.

Andrews, D. J., S. W. H. Cowley, M. K. Dougherty, L. Lamy, G. Provan, and D. J. Southwood (2012), Planetary period oscillations in Saturn's magnetosphere: Evolution of magnetic oscillation properties from southern summer to post-equinox, *J. Geophys. Res.*, 117, A04224, doi:10.1029/2011JA017444.

Arridge, C. S., J. M. Jasinski, N. Achilleos, Y. V. Bogdanova, E. J. Bunce, S. W. H. Cowley, A. N. Fazakerley, K. K. Khurana, L. Lamy, J. S. Leisner, et al. (2016), Cassini observations of Saturn's southern polar cusp, *J. Geophys. Res. Space Physics*, 121, 3006–3030, doi:10.1002/2015JA021957.

Badman, S. V., N. Achilleos, K. H. Baines, R. H. Brown, E. J. Bunce, M. K. Dougherty, H. Melin, J. D. Nichols, and T. Stallard (2011), Location of Saturn's northern infrared aurora determined from Cassini VIMS images, *Geophys. Res. Lett.*, 38, L03102, doi:10.1029/2010GL046193.

Badman, S. V., et al. (2012), Rotational modulation and local time dependence of Saturn's infrared H_3^+ auroral intensity, *J. Geophys. Res.*, 117, A09228, doi:10.1029/2012JA017990.

Badman, S. V., A. Masters, H. Hasegawa, M. Fujimoto, A. Radioti, D. Grodent, N. Sergis, M. K. Dougherty, and A. J. Coates (2013), Bursty magnetic reconnection at Saturn's magnetopause, *Geophys. Res. Lett.*, 40, 1027–1031, doi:10.1002/grl.50199.

Badman, S. V., et al. (2016), Saturn's auroral morphology and field-aligned currents during a solar wind compression, *Icarus*, 263, 83–93, doi:10.1016/j.icarus.2014.11.014.

Belenkaya, E. S., S. W. H. Cowley, C. J. Meredith, J. D. Nichols, V. V. Kalegaev, I. I. Alexeev, O. G. Barinov, W. O. Barinova, and M. S. Blokhina (2014), Magnetospheric magnetic field modelling for the 2011 and 2012 HST Saturn aurora campaigns – implications for auroral source regions, *Ann. Geophys.*, 32, 689–704, doi:10.5194/angeo-32-689-2014, 2014.

Bunce, E. J., et al. (2008), Origin of Saturn's aurora: Simultaneous observations by Cassini and the Hubble Space Telescope, *J. Geophys. Res.*, 113, A09209, doi:10.1029/2008JA013257.

Bunce, E. J., et al. (2014), Cassini nightside observations of the oscillatory motion of Saturn's northern auroral oval, *J. Geophys. Res. Space Physics*, 119, 3528–3543, doi:10.1002/2013JA019527.

Carbary, J. F. (2012), The morphology of Saturn's ultraviolet aurora, *J. Geophys. Res.*, 117, A06210, doi:10.1029/2012JA017670.

Carbary, J. F. (2013), Longitude dependences of Saturn's ultraviolet aurora, *Geophys. Res. Lett.*, 40, 1920–1906, doi:10.1002/grl.50430.

Carbary, J. F., and D. G. Mitchell (2013), Periodicities in Saturn's magnetosphere, *Rev. Geophys.*, 51, 1–30, doi:10.1002/rog.20006.

Clarke, J. T., et al. (2009), Response of Jupiter's and Saturn's auroral activity to the solar wind, *J. Geophys. Res.*, 114, A05210, doi:10.1029/2008JA013694.

Cowley, S. W. H. and E. J. Bunce (2003), Corotation-driven magnetosphere-ionosphere coupling currents in Saturn's magnetosphere and their relation to the auroras, *Ann. Geophys.*, 21, 1691-1707, doi:10.5194/angeo-21-1691-2003.

Cowley, S. W. H., E. J. Bunce, and J. M. O'Rourke (2004a), A simple quantitative model of plasma flows and currents in Saturn's polar ionosphere, *J. Geophys. Res.*, 109, A05212, doi:10.1029/2003JA010375.

Cowley, S. W. H., E. J. Bunce, and R. Prangé (2004b), Saturn's polar ionospheric flows and their relation to the main auroral oval, *Ann. Geophys.*, 22, 1379-1394, doi:10.5194/angeo-22-1379-2004.

Cowley, S. W. H., S. V. Badman, E. J. Bunce, J. T. Clarke, J.-C. Gérard, D. Grodent, C. M. Jackman, S. E. Milan, and T. K. Yeoman (2005), Reconnection in a rotation-dominated magnetosphere and its relation to Saturn's auroral dynamics, *J. Geophys. Res.*, 110, A02201, doi:10.1029/2004JA010796.

Cowley, S. W. H., C. S. Arridge, E. J. Bunce, J. T. Clarke, A. J. Coates, M. K. Dougherty, J.-C. Gérard, D. Grodent, J. D. Nichols, and D. L. Talboys (2008), Auroral current systems in Saturn's magnetosphere: comparison of theoretical models with Cassini and HST observations, *Ann. Geophys.*, 26, 2613-2630, doi:10.5194/angeo-26-2613-2008.

Cowley, S. W. H. & G. Provan (2016), Planetary period oscillations in Saturn's magnetosphere: Further comments on the relationship between post-equinox properties deduced from magnetic field and Saturn kilometric radiation measurements, *Icarus*, 272, 258-276, doi:10.1016/j.icarus.2016.02.051.

Espinosa, S. A., & M. K. Dougherty (2000), Periodic perturbations in Saturn's magnetic field, *Geophys. Res. Lett.*, 27 (17), doi:10.1029/2000GL000048.

Fischer, G., D. A. Gurnett, W. S. Kurth, S.-Y. Ye, J. B. Groene (2015), Saturn kilometric radiation periodicity after equinox, *Icarus*, 254, 72-91, doi:10.1016/j.icarus.2015.03.014.

Galopeau, P. H. M., P. Zarka, and D. Le Quéau (1995), Source location of Saturn's kilometric radiation: The Kelvin-Helmholtz instability hypothesis, *J. Geophys. Res.*, 100(E12), 26397–26410, doi:10.1029/95JE02132.

Gérard, J.-C., D. Grodent, J. Gustin, A. Saglam, J. T. Clarke, and J. T. Trauger (2004), Characteristics of Saturn's FUV aurora observed with the Space Telescope Imaging Spectrograph, *J. Geophys. Res.*, 109, A09207, doi:10.1029/2004JA010513.

Gérard, J.-C., E. J. Bunce, D. Grodent, S. W. H. Cowley, J. T. Clarke, and S. V. Badman (2005), Signature of Saturn's auroral cusp: Simultaneous Hubble Space Telescope FUV observations and upstream solar wind monitoring, *J. Geophys. Res.*, 110, A11201, doi:10.1029/2005JA011094.

Gérard, J.-C., B. Bonfond, J. Gustin, D. Grodent, J. T. Clarke, D. Bisikalo, and V. Shematovich (2009), Altitude of Saturn's aurora and its implications for the characteristic energy of precipitated electrons, *Geophys. Res. Lett.*, 36, L02202, doi:10.1029/2008GL036554.

- Grodent, D., J.-C. Gérard, S. W. H. Cowley, E. J. Bunce, and J. T. Clarke (2005), Variable morphology of Saturn's southern ultraviolet aurora, *J. Geophys. Res.*, 110, A07215, doi:10.1029/2004JA010983.
- Grodent, D., A. Radioti, B. Bonfond, and J.-C. Gérard (2010), On the origin of Saturn's outer auroral emission, *J. Geophys. Res.*, 115, A08219, doi:10.1029/2009JA014901.
- Grodent, D., J. Gustin, J.-C. Gérard, A. Radioti, B. Bonfond, and W. R. Pryor (2011), Small-scale structures in Saturn's ultraviolet aurora, *J. Geophys. Res.*, 116, A09225, doi:10.1029/2011JA016818.
- Gurnett, D. A., A. Lecacheux, W. S. Kurth, A. M. Persoon, J. B. Groene, L. Lamy, P. Zarka, and J. F. Carbary (2009), Discovery of a north-south asymmetry in Saturn's radio rotation period, *Geophys. Res. Lett.*, 36, L16102, doi:10.1029/2009GL039621.
- Gurnett, D. A., J. B. Groene, A. M. Persoon, J. D. Meniotti, S.-Y. Ye, W. S. Kurth, R. J. MacDowall, and A. Lecacheux (2010), The reversal of the rotational modulation rates of the north and south components of Saturn kilometric radiation near equinox, *Geophys. Res. Lett.*, 37, L24101, doi:10.1029/2010GL045796
- Gustin, J., B. Bonfond, D. Grodent, and J.-C. Gérard (2012), Conversion from HST ACS and STIS auroral counts into brightness, precipitated power, and radiated power for H₂ giant planets, *J. Geophys. Res.*, 117, A07316, doi:10.1029/2012JA017607.
- Hill, T. W., A. M. Rymer, J. L. Burch, F. J. Crary, D. T. Young, M. F. Thomsen, D. Delapp, N. André, A. J. Coates, and G. R. Lewis (2005), Evidence for rotationally driven plasma transport in Saturn's magnetosphere, *Geophys. Res. Lett.*, 32, L14S10, doi:10.1029/2005GL022620.
- Hunt, G. J., S. W. H. Cowley, G. Provan, E. J. Bunce, I. I. Alexeev, E. S. Belenkaya, V. V. Kalegaev, M. K. Dougherty, and A. J. Coates (2015a), Field-aligned currents in Saturn's southern nightside magnetosphere: Subcorotation and planetary period oscillation components, *J. Geophys. Res. Space Physics*, 119, 9847-9899, doi:10.1002/2014JA020506.
- Hunt, G. J., S. W. H. Cowley, G. Provan, E. J. Bunce, I. I. Alexeev, E. S. Belenkaya, V. V. Kalegaev, M. K. Dougherty, and A. J. Coates (2015b), Field-aligned currents in Saturn's northern nightside magnetosphere: Evidence for interhemispheric current flow associated with planetary period oscillations, *J. Geophys. Res. Space Physics*, 120, 7552–7584, doi:10.1002/2015JA021454.
- Hunt, G. J., S. W. H. Cowley, G. Provan, E. J. Bunce, I. I. Alexeev, E. S. Belenkaya, V. V. Kalegaev, M. K. Dougherty, and A. J. Coates (2016), Field-aligned currents in Saturn's magnetosphere: Local time dependence of southern summer currents in the dawn sector between midnight and noon, *J. Geophys. Res. Space Physics*, 121, 7785–7804, doi:10.1002/2016JA022712.
- Jackman C. M., N. Achilleos, S. W. H. Cowley, E. J. Bunce, A. Radioti, D. Grodent, S. V. Badman, M. K. Dougherty, and W. Pryor (2013), Auroral counterpart of magnetic field dipolarizations in Saturn's tail, *Planetary and Space Science*, 82–83, 34-42, doi:10.1016/j.pss.2013.03.010.
- Kaiser, M.L., M.D. Desch, J.W. Warwick, and J.B. Pearce (1980), Voyager detection of non- thermal radio emission from Saturn, *Science*, 209, 1238–1240, doi: 10.1126/science.209.4462.1238.
- Kaiser, M. L., and M. D. Desch (1982), Saturnian kilometric radiation: Source locations, *J. Geophys. Res.*, 87(A6), 4555–4559, doi:10.1029/JA087iA06p04555.
- Kinrade, J., et al. (2017), An isolated, bright cusp aurora at Saturn, *J. Geophys. Res. Space Physics*, 122, 6121–6138, doi:10.1002/2016JA023792.

Kurth, W. S., T. F. Averkamp, D. A. Gurnett, J. B. Groene, and A. Lecacheux (2008), An update to a Saturnian longitude system based on kilometric radio emissions, *J. Geophys. Res.*, 113, A05222, doi:10.1029/2007JA012861.

Lamy, L., P. Zarka, B. Cecconi, R. Prangé, W. S. Kurth, and D. A. Gurnett (2008), Saturn kilometric radiation: Average and statistical properties, *J. Geophys. Res.*, 113, A07201, doi:10.1029/2007JA012900.

Lamy, L., B. Cecconi, R. Prangé, P. Zarka, J. D. Nichols, and J. T. Clarke (2009), An auroral oval at the footprint of Saturn's kilometric radio sources, collocated with the UV aurorae, *J. Geophys. Res.*, 114, A10212, doi:10.1029/2009JA014401.

Lamy, L., et al. (2010), Properties of Saturn kilometric radiation measured within its source region, *Geophys. Res. Lett.*, 37, L12104, doi:10.1029/2010GL043415.

Lamy, L. (2011), Variability of southern and northern SKR periodicities. In: Rucker, H. O. (Ed.), *Proceedings of the Seventh International Workshop on Planetary, Solar, and Heliospheric Radio Emissions*. Austrian Acad. Sci., Vienna, 39–50, doi:10.1553/PRE7s39.

Lamy, L., R. Prangé, W. Pryor, J. Gustin, S. V. Badman, H. Melin, T. Stallard, D. G. Mitchell, and P. C. Brandt (2013), Multispectral simultaneous diagnosis of Saturn's aurorae throughout a planetary rotation, *J. Geophys. Res. Space Physics*, 118, 4817–4843, doi:10.1002/jgra.50404.

Lamy, L. (2017), The Saturnian Kilometric Radiation before the Cassini Grand Finale, *Proceedings of the 8th International Workshop on Planetary, Solar and Heliospheric Radio Emissions (PRE VIII)*, Seggau, Austria, Oct. 25-27, 2016.

Masters, A., et al. (2010), Cassini observations of a Kelvin-Helmholtz vortex in Saturn's outer magnetosphere, *J. Geophys. Res.*, 115, A07225, doi:10.1029/2010JA015351.

Meredith, C. J., S. W. H. Cowley, K. C. Hansen, J. D. Nichols, and T. K. Yeoman (2013), Simultaneous conjugate observations of small-scale structures in Saturn's dayside ultraviolet auroras: Implications for physical origins, *J. Geophys. Res. Space Physics*, 118, 2244–2266, doi:10.1002/jgra.50270.

Meredith, C. J., I. I. Alexeev, S. V. Badman, E. S. Belenkaya, S. W. H. Cowley, M. K. Dougherty, V. V. Kalegaev, G. R. Lewis, and J. D. Nichols (2014), Saturn's dayside ultraviolet auroras: Evidence for morphological dependence on the direction of the upstream interplanetary magnetic field, *J. Geophys. Res. Space Physics*, 119, 1994–2008, doi:10.1002/2013JA019598.

Meredith, C. J., S. W. H. Cowley, and J. D. Nichols (2015), Survey of Saturn auroral storms observed by the Hubble Space Telescope: Implications for storm time scales, *J. Geophys. Res. Space Physics*, 119, 9624–9642, doi:10.1002/2014JA020601.

Mitchell, D. G., S.M. Krimigis, C. Paranicas, P.C. Brandt, J.F. Carbary, E.C. Roelof, W.S. Kurth, D.A. Gurnett, J.T. Clarke, J.D. Nichols, J.-C. Gérard, D.C. Grodent, M.K. Dougherty, and W.R. Pryor (2009), Recurrent energization of plasma in the midnight-to-dawn quadrant of Saturn's magnetosphere, and its relationship to auroral UV and radio emissions, *Planetary and Space Science*, 57 (14-15), 1732-1742, doi:10.1016/j.pss.2009.04.002.

Mitchell, D. G., P. C. Brandt, J. F. Carbary, W. S. Kurth, S. M. Krimigis, C. Paranicas, N. Krupp, D. C. Hamilton, B. H. Mauk, G. B. Hospodarsky, M. K. Dougherty, and W. R. Pryor (2015), Injection, Interchange, and Reconnection, in *Magnetotails in the Solar System* (eds A. Keiling, C. M. Jackman and P. A. Delamere), John Wiley & Sons, Inc, Hoboken, NJ. doi:10.1002/9781118842324.ch19.

Mitchell, D. G., J.F. Carbary, E.J. Bunce, A. Radioti, S.V. Badman, W.R. Pryor, G.B. Hospodarsky, and W.S. Kurth (2016), Recurrent pulsations in Saturn's high latitude magnetosphere, *Icarus*, 263, 94-100, doi:10.1016/j.icarus.2014.10.028.

Nichols, J. D., J. T. Clarke, S. W. H. Cowley, J. Duval, A. J. Farmer, J.-C. Gérard, D. Grodent, and S. Wannawichian (2008), Oscillation of Saturn's southern auroral oval, *J. Geophys. Res.*, 113, A11205, doi:10.1029/2008JA013444.

Nichols, J. D., et al. (2009), Saturn's equinoctial auroras, *Geophys. Res. Lett.*, 36, L24102, doi:10.1029/2009GL041491.

Nichols, J. D., B. Cecconi, J. T. Clarke, S. W. H. Cowley, J.-C. Gérard, A. Grocott, D. Grodent, L. Lamy, and P. Zarka (2010a), Variation of Saturn's UV aurora with SKR phase, *Geophys. Res. Lett.*, 37, L15102, doi:10.1029/2010GL044057.

Nichols, J. D., S. W. H. Cowley, and L. Lamy (2010b), Dawn-dusk oscillation of Saturn's conjugate auroral ovals, *Geophys. Res. Lett.*, 37, L24102, doi:10.1029/2010GL045818.

Nichols, J. D., et al. (2014), Dynamic auroral storms on Saturn as observed by the Hubble Space Telescope, *Geophys. Res. Lett.*, 41, 3323–3330, doi:10.1002/2014GL060186.

Nichols, J.D., S.V. Badman, E.J. Bunce, J.T. Clarke, S.W.H. Cowley, G.J. Hunt, and G. Provan (2016), Saturn's northern auroras as observed using the Hubble Space Telescope, *Icarus*, 263, 17-31, doi:10.1016/j.icarus.2015.09.008.

Prangé, R., L. Pallier, K. C. Hansen, R. Howard, A. Vourlidis, R. Courtin, and C. Parkinson (2004), An interplanetary shock traced by planetary auroral storms from the Sun to Saturn, *Nature*, 432, 78-81, doi:10.1038/nature02986.

Provan, G., D. J. Andrews, C. S. Arridge, A. J. Coates, S. W. H. Cowley, S. E. Milan, M. K. Dougherty, and D. M. Wright (2009a), Polarization and phase of planetary-period magnetic field oscillations on high-latitude field lines in Saturn's magnetosphere, *J. Geophys. Res. Space Physics*, 114 (2), doi:10.1029/2008JA013782.

Provan, G., S. W. H. Cowley, and J. D. Nichols (2009b), Phase relation of oscillations near the planetary period of Saturn's auroral oval and the equatorial magnetospheric magnetic field, *J. Geophys. Res.*, 114, A04205, doi:10.1029/2008JA013988.

Provan, G., D. J. Andrews, B. Cecconi, S. W. H. Cowley, M. K. Dougherty, L. Lamy, and P. M. Zarka (2011), Magnetospheric period magnetic field oscillations at Saturn: Equatorial phase "jitter" produced by superposition of southern and northern period oscillations, *J. Geophys. Res.*, 116, A04225, doi:10.1029/2010JA016213.

Provan, G., S. W. H. Cowley, J. Sandhu, D. J. Andrews, and M. K. Dougherty (2013), Planetary period magnetic field oscillations in Saturn's magnetosphere: Postequinox abrupt nonmonotonic transitions to northern system dominance, *J. Geophys. Res. Space Physics*, 118, 3243–3264, doi:10.1002/jgra.50186.

Provan, G., L. Lamy, S. W. H. Cowley, and M. K. Dougherty (2014), Planetary period oscillations in Saturn's magnetosphere: Comparison of magnetic oscillations and SKR modulations in the postequinox interval, *J. Geophys. Res. Space Physics*, 119, 7380–7401, doi:10.1002/2014JA020011.

Provan, G., C. Tao, S. W. H. Cowley, M. K. Dougherty, and A. J. Coates (2015), Planetary period oscillations in Saturn's magnetosphere: Examining the relationship between abrupt changes in

behavior and solar wind-induced magnetospheric compressions and expansions, *J. Geophys. Res. Space Physics*, 120, 9524–9544, doi:10.1002/2015JA021642.

Provan, G., S.W.H. Cowley, L. Lamy, E.J. Bunce, G.J. Hunt, P. Zarka, and M.K. Dougherty (2016), Planetary period oscillations in Saturn's magnetosphere: Coalescence and reversal of northern and southern periods in late northern spring, *J. Geophys. Res. Space Physics*, 121, 9829–9862, doi:10.1002/2016JA023056.

Radioti, A., D. Grodent, J.-C. Gérard, S. E. Milan, B. Bonfond, J. Gustin, and W. Pryor (2011), Bifurcations of the main auroral ring at Saturn: ionospheric signatures of consecutive reconnection events at the magnetopause, *J. Geophys. Res.*, 116, A11209, doi:10.1029/2011JA016661.

Radioti, A., E. Roussos, D. Grodent, J.-C. Gérard, N. Krupp, D. G. Mitchell, J. Gustin, B. Bonfond, and W. Pryor (2013), Signatures of magnetospheric injections in Saturn's aurora, *J. Geophys. Res. Space Physics*, 118, 1922–1933, doi:10.1002/jgra.50161.

Sandel, B. R., et al. (1982), Extreme ultraviolet observations from the Voyager 2 encounter with Saturn, *Science*, 215 (4532), 548-553. Doi:10.1126/science.215.4532.548.

Southwood, D. J., and M. G. Kivelson (2007), Saturnian magnetospheric dynamics: Elucidation of a camshaft model, *J. Geophys. Res.*, 112, A12222, doi:10.1029/2007JA012254.

Southwood, D. (2011), Direct evidence of differences in magnetic rotation rate between Saturn's northern and southern polar regions, *J. Geophys. Res.*, 116, A01201, doi:10.1029/2010JA016070.

Vasyliunas, V. M. (1983), Plasma distribution and flow, in *Physics of the Jovian Magnetosphere* (ed. A. J. Dessler), Cambridge Univ. Press, Cambridge, UK, p. 395–453, 1983.

Yao Z. et al., (2017), Mechanisms of Saturn's near-noon transient aurora: in situ evidence from Cassini measurements, *Geophys. Res. Lett.*, 44, doi:10.1002/2017GL075108.

Zarka, P., L. Lamy, B. Cecconi, R. Prangé, and H. O. Rucker (2007), Modulation of Saturn's radio clock by solar wind speed, *Nature*, 450, 265-267, doi:10.1038/nature06237.

Accepted Article

Table 1. Mean colatitudes (θ) and associated standard deviations (σ) in degrees for the northern equatorward and poleward boundaries (subscripts ‘*eq*’ and ‘*pl*’, respectively), over 10° longitude bins centred on angle ϕ_{LT} increasing anti-clockwise from zero at midnight. Dawn-arc region values are gray-shaded.

| j_{LT}° (LT) | $\langle q_{eq} \rangle$ | S_{eq} | $\langle q_{pl} \rangle$ | S_{pl} |
|---------------------|--------------------------|----------|--------------------------|----------|
| 45 (03:00) | 18.8 | 0.9 | 15.3 | 1.0 |
| 55 (03:40) | 18.0 | 0.8 | 15.2 | 0.8 |
| 65 (04:20) | 17.1 | 0.5 | 15.0 | 0.6 |
| 75 (05:00) | 16.3 | 1.0 | 14.5 | 1.1 |
| 85 (05:40) | 16.0 | 1.0 | 14.2 | 1.1 |
| 95 (06:20) | 15.7 | 0.9 | 13.9 | 1.0 |
| 105 (07:00) | 15.4 | 0.8 | 13.6 | 0.9 |
| 115 (07:40) | 15.4 | 0.8 | 13.4 | 0.9 |
| 125 (08:20) | 15.0 | 1.0 | 12.7 | 1.1 |
| 135 (09:00) | 14.8 | 0.8 | 12.8 | 1.1 |
| 145 (09:40) | 14.5 | 2.3 | 11.3 | 1.9 |
| 155 (10:20) | 13.4 | 1.9 | 10.3 | 2.0 |
| 165 (11:00) | 11.3 | 1.2 | 7.9 | 1.6 |
| 175 (11:40) | 11.4 | 2.0 | 8.1 | 2.0 |
| 185 (12:20) | 11.6 | 1.4 | 8.4 | 1.3 |
| 195 (13:00) | 11.1 | 1.5 | 8.1 | 1.4 |
| 205 (13:40) | 11.7 | 2.2 | 8.3 | 1.7 |
| 215 (14:20) | 9.9 | 3.1 | 7.8 | 2.5 |
| 225 (15:00) | 12.1 | 3.4 | 8.3 | 2.3 |
| 235 (15:40) | 10.3 | 3.3 | 6.3 | 1.0 |
| 245 (16:20) | 11.9 | 3.5 | 8.2 | 2.4 |
| 255 (17:00) | 11.8 | 3.0 | 8.8 | 3.0 |
| 265 (17:40) | 13.6 | 2.7 | 11.0 | 3.2 |
| 275 (18:20) | 15.0 | 2.3 | 12.3 | 2.8 |
| 285 (19:00) | 15.3 | 2.4 | 12.5 | 2.4 |
| 295 (19:40) | 16.6 | 2.1 | 12.8 | 2.4 |
| 305 (20:20) | 17.0 | 2.0 | 12.6 | 1.6 |
| 315 (21:00) | 18.6 | 0.9 | 14.0 | 1.6 |
| Overall | 15.0 | 2.8 | 12.4 | 3.0 |

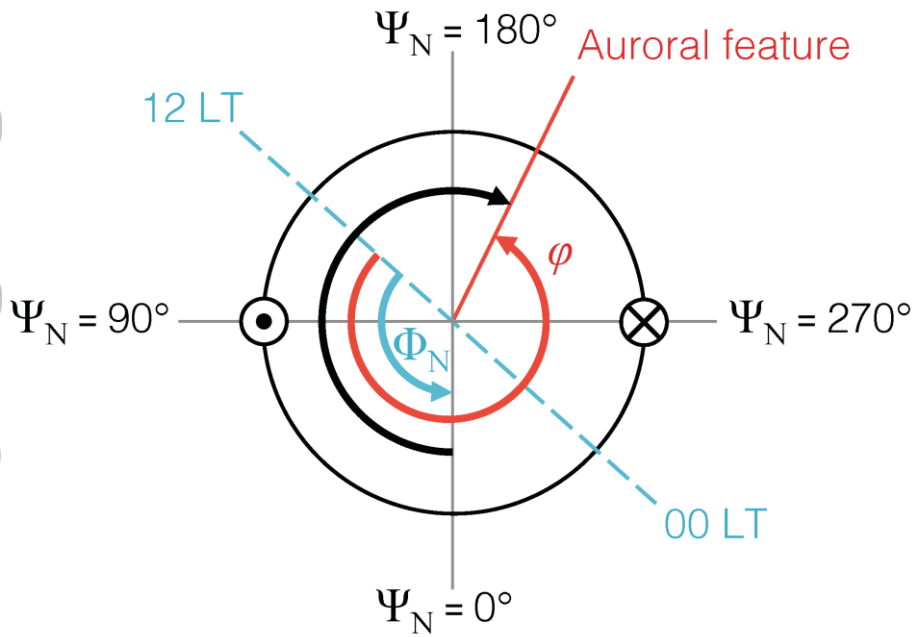


Figure 1. A diagram illustrating the northern magnetic longitude system, Ψ_N , with respect to the PPO dipole angle, Φ_N , at an arbitrary time. The PPO dipole angle (or phase) is defined from noon (labeled 12 LT) and proceeds anti-clockwise as the system rotates with near-planetary period. An auroral feature has a magnetic longitude of Ψ_N , the clockwise angle from the PPO model dipole position at Φ_N . The magnetic longitude of an auroral feature fixed in local time therefore increases as the system rotates. Regions of expected maximum upward (dot) and downward (cross) field-aligned PPO current associated with the primary northern hemisphere system are also labeled, at $\Psi_N = 90^\circ$ and $\Psi_N = 270^\circ$ respectively.

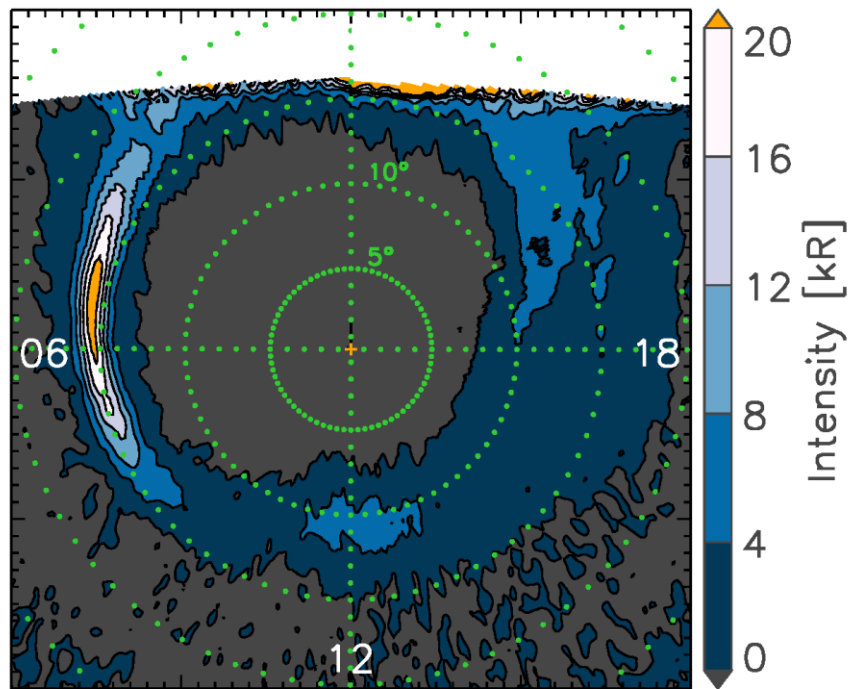


Figure 2. Mean northern FUV intensity from the 2014 HST campaign, in polar projection and a fixed local time frame. A region close to the planetary limb has been clipped from the image in this projection (white area at top) to remove distorted pixels at oblique viewing angles (the increased intensity along the cropped edge of the contours is an image artefact). Local time sectors are labeled in white at 06, 12 and 18 LT, and green dots along these principal meridians have 1° latitude spacing. Rings of constant co-latitude are shown at 5° , 10° , 15° and 20° by green dots with 5° longitude spacing.

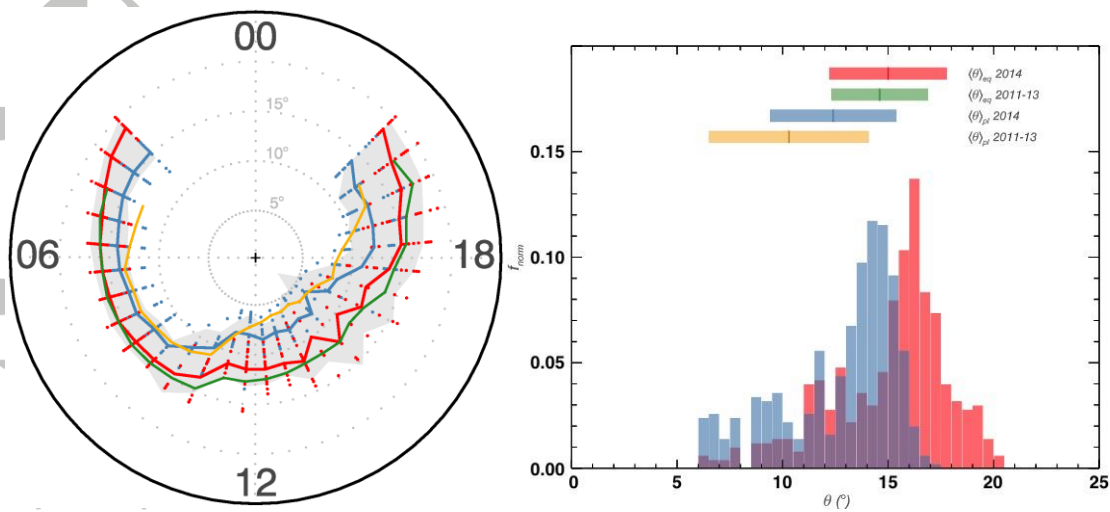


Figure 3. 3a: A fixed LT, polar projection showing equatorward (red dots) and poleward (blue dots) auroral colatitude boundaries determined from HST FUV images of Saturn's northern hemisphere in 2014. Emission intensity was averaged in 10° longitude bins, and Gaussian fits were obtained for each latitudinal profile. Boundary points were taken as the latitudinal intersect of the Gaussian curve's FWHM. Solid lines show the resulting mean auroral boundaries (equatorward in red, poleward in blue), together with equivalent boundaries from 2011-13 HST campaigns (equatorward in green, and poleward in yellow) as reported by Nichols et al., (2016). **3b:** Normalised histogram showing the colatitude distribution of equatorward (red) and poleward (blue) auroral boundaries shown in Figure 3a. The horizontal colored bars above the histogram indicate the mean equatorward and poleward boundaries and $\pm 1-\sigma$ ranges from 2014 (red, blue, see Table 2) and 2011-13 campaigns (green, yellow, see Nichols et al., 2016).

Accepted

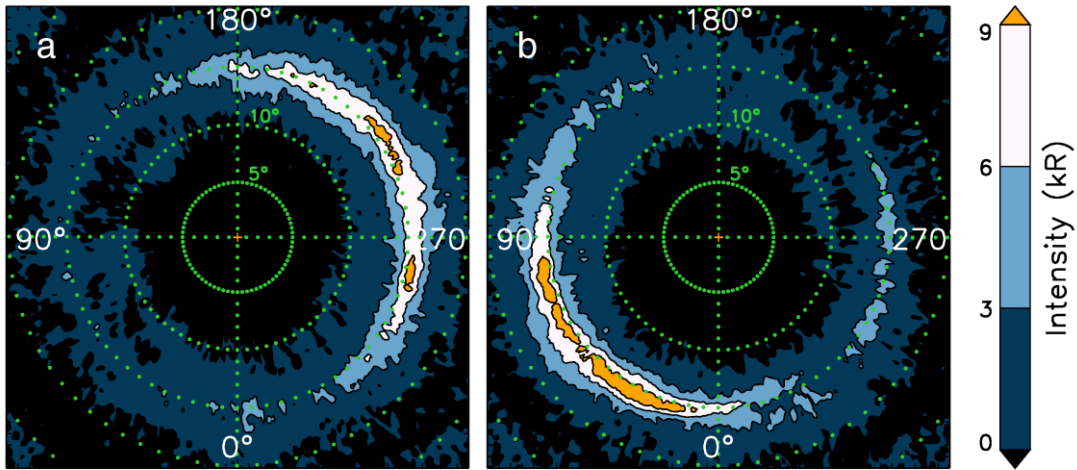


Figure 4. Mean intensity of the northern FUV auroral emission in the (4a) northern and (4b) southern magnetic longitude (Ψ) frames, obtained from all 60 exposures in the 2014 HST campaign. Dark gray shading shows where average image intensity is < 0 kR, resulting from over-estimation of the planetary limb background removal outside the auroral emission region. Green dots along the principal local time meridians have 1° latitude spacing, and rings of constant latitude are shown by dots with 5° longitude spacing.

Accepted Article

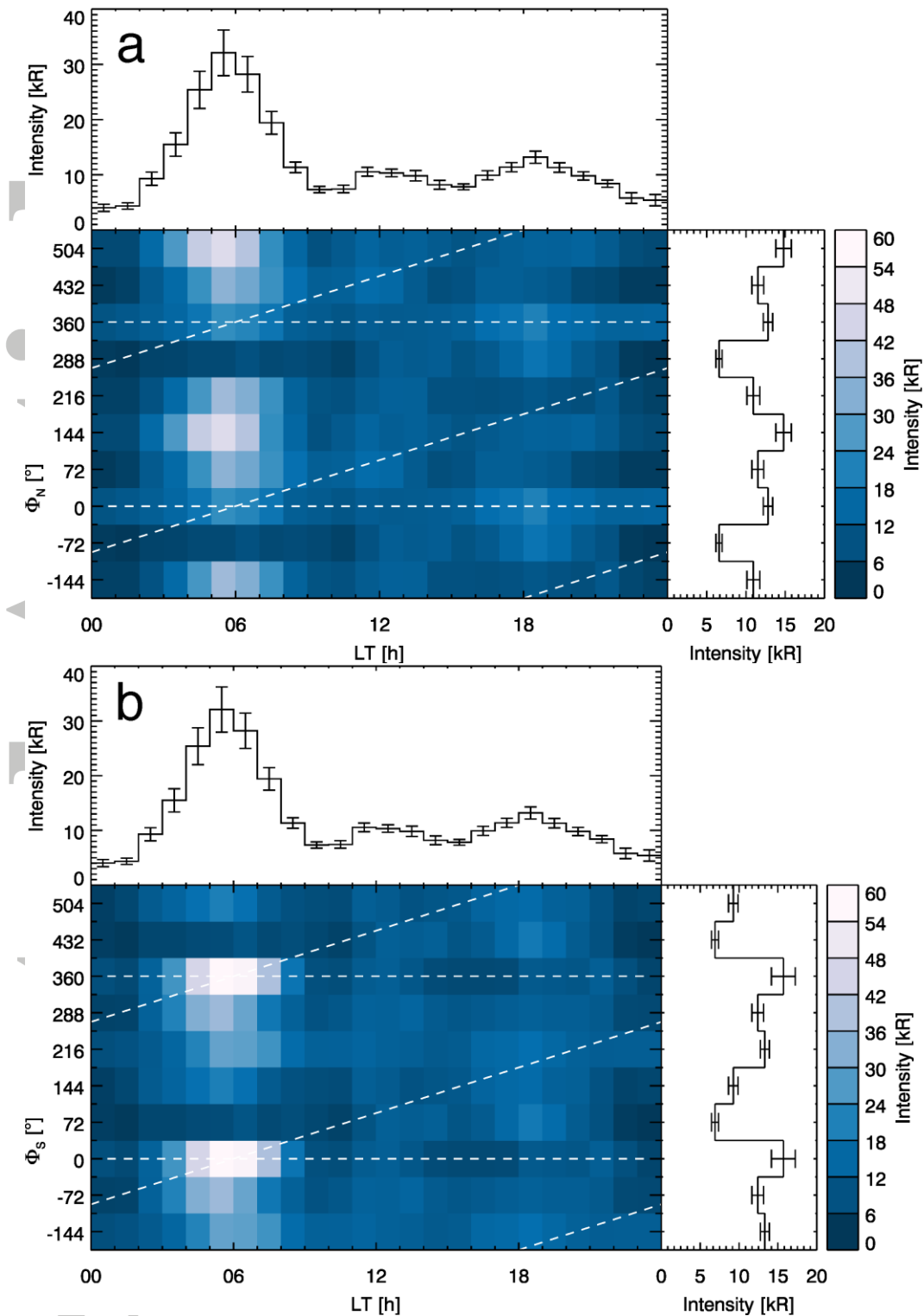


Figure 5. Maximum northern FUV intensities as a function of LT (1 h bins) and PPO phase (Φ , 72° bins) for the northern (**5a**) and southern (**5b**) systems. Two complete PPO phase cycles are plotted vertically to highlight periodicity (horizontal white dash lines mark phases at 0° and 360°). The line plots in the top and side panels show the average maximum intensities across the local time and dipole phase bins respectively. Error bars in each line plot indicate the standard deviation around the bin average. Diagonal dash lines show the magnetic longitude position at which upward current is expected to maximize in the northern hemisphere according to the PPO system model i.e. $\Psi_{N,S} = 90^\circ$.

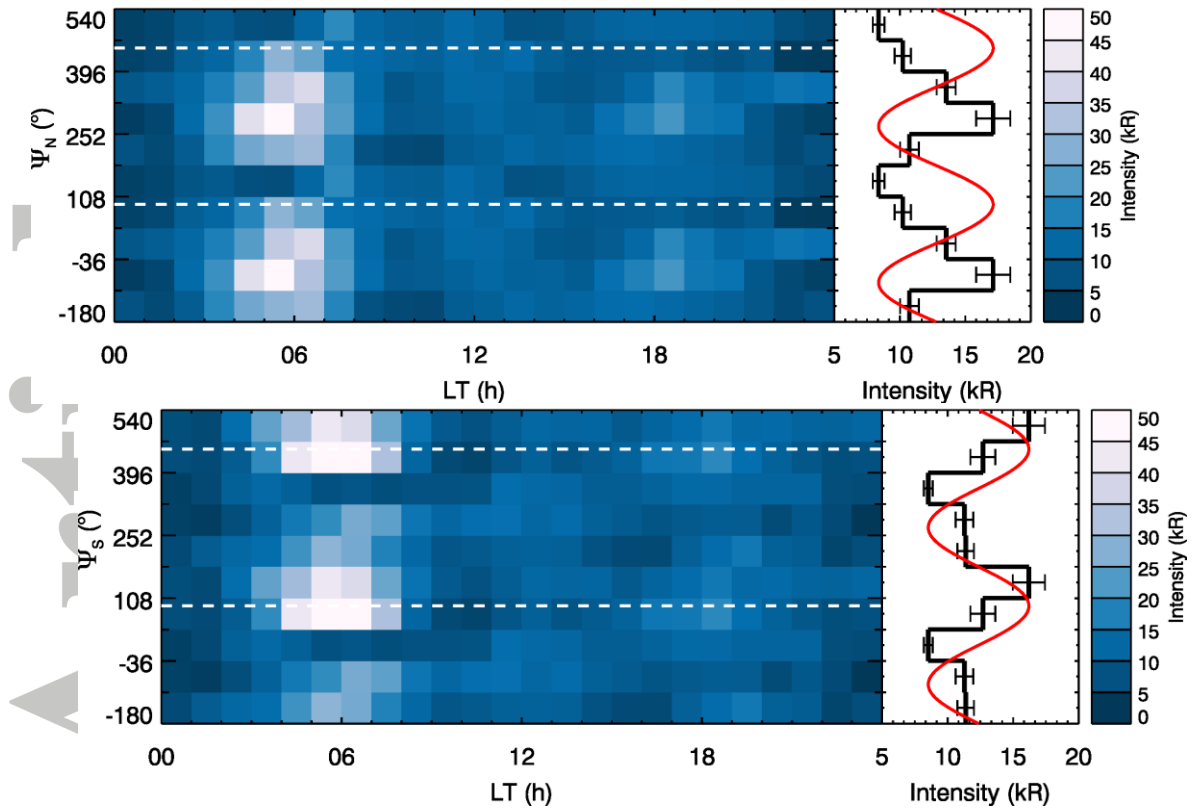


Figure 6. Maximum northern auroral intensities as a function of LT (1 h bins) and northern (**6a**) and southern (**6b**) magnetic longitude, Ψ (72° bins). The right panels show the mean overall intensity within each longitude bin, plotted together with standard error bars. The red sinusoids show the expected longitudinal modulation pattern in the northern hemisphere from the northern primary (**6a**) and southern interhemispheric (**6b**) upward FACs, peaking at $\Psi_{N,S} = 90^\circ$ respectively, scaled in each case to the mean intensity response. White dash lines show the magnetic longitude at which upward current is expected to maximize in the northern hemisphere according to the PPO system model i.e. $\Psi_{N,S} = 90^\circ$.

Accepted

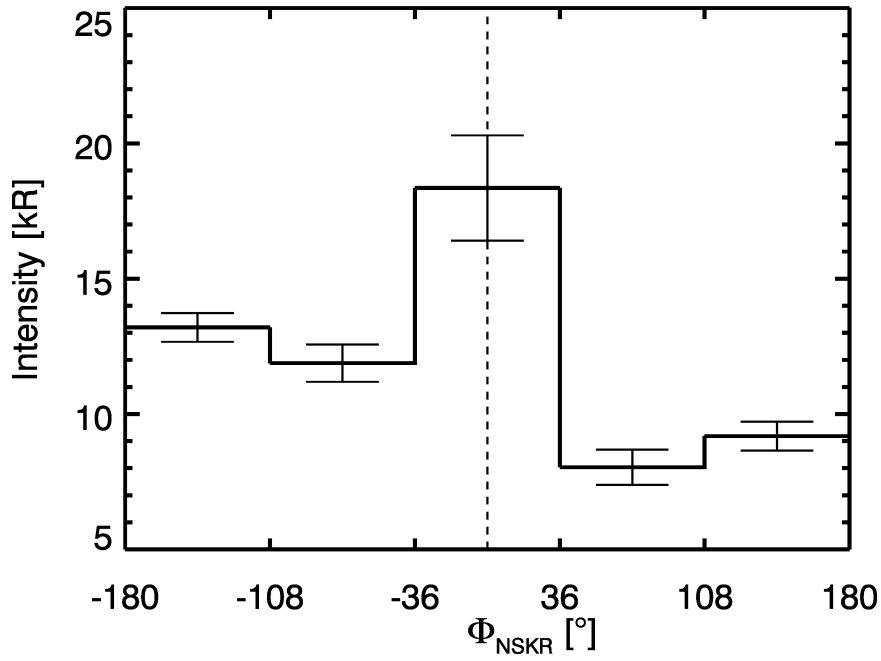


Figure 7. A histogram of maximum auroral intensity between 10-20° colatitude versus northern SKR phase, Φ_{NSKR} . Phase bins are 72° wide, and the plot is centred on $\Phi_{\text{NSKR}} = 0^\circ$ (vertical dash line), where UV emission power is expected to maximize around a dawn source region. Vertical error bars show the standard deviation in intensity within the SKR phase bins.

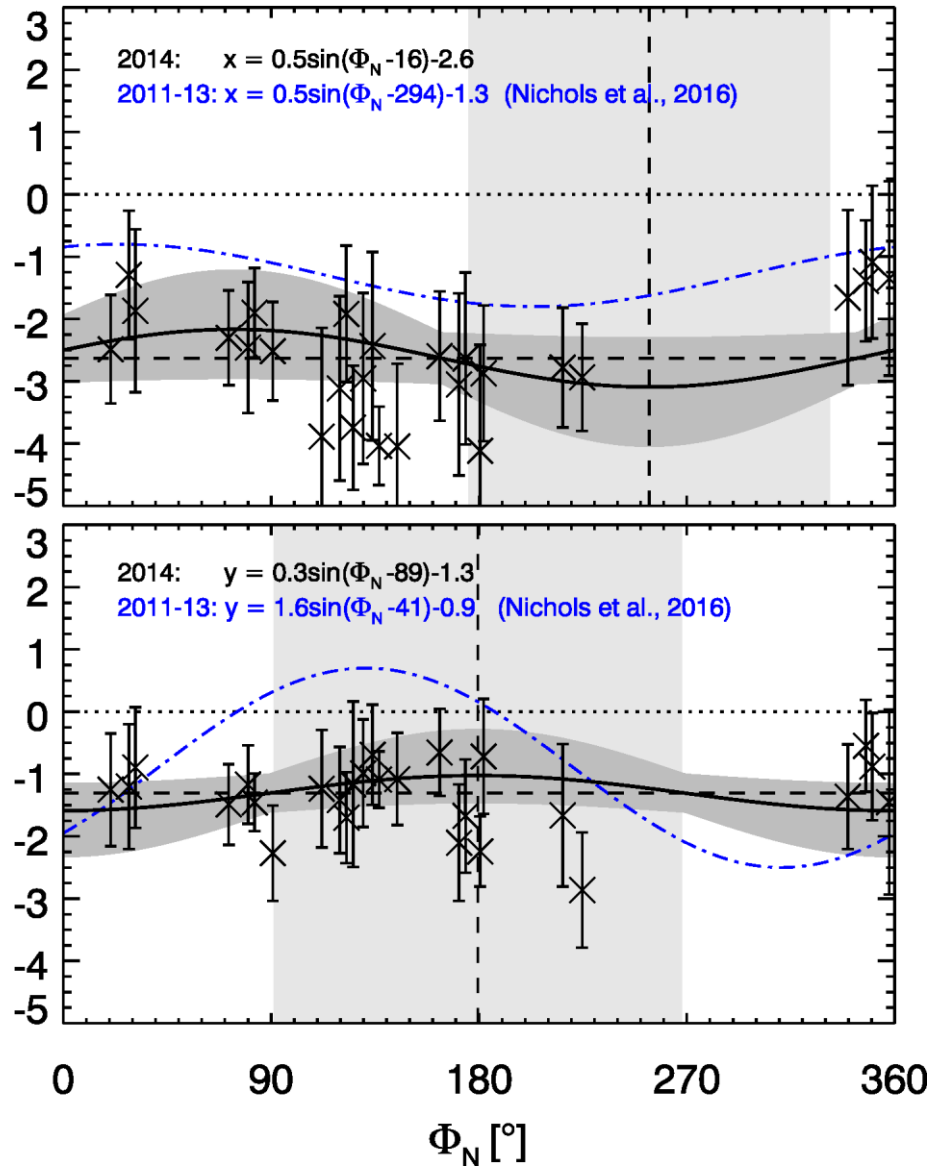


Figure 8. Locations of circle centres (in degrees of colatitude) based on fits of the northern auroras in the x (top panel, positive sunward) and y (bottom panel, positive duskward) direction versus northern PPO dipole phase, Φ_N . Error bars show uncertainty in the circle fit, based on the sum-square mean distance of the boundary points from the circle. Best-fit sinusoids are plotted in solid black lines, with their equations shown in the top left of each panel. The dark grey shaded regions indicate the combined 1-sigma uncertainties in the amplitude and vertical offset parameters of the fit. Vertical dash lines show the maximum anti-sunward (top panel) and duskward (bottom panel) displacement respectively, with the light grey region indicating the 1-sigma uncertainty in the phase offset parameter of the fit. The boundary detection and circle fitting methods used here are described by Nichols et al. (2016), who performed this same analysis on northern auroral images from HST campaigns in 2011-13. The best-fit circle centre locations from Nichols et al. (2016) are shown for comparison with blue dot-dash lines and equations.